

Architecture for space-based exoplanet spectroscopy in the mid-infrared

Joseph Green*, Case Bradford, Thomas Gautier, Michael Rodgers, Erkin Sidick and Gautam Vasisht
Jet Propulsion Laboratory, California Institute of Technology, 4800 Oak Grove Drive, Pasadena, CA 91109

ABSTRACT

Characterizing exoearths at wavelength about 10 micron offers many benefits over visible coronagraphy. Apart from providing direct access to a number of significant bio-signatures, direct-imaging in the mid-infrared can provides 1000 times or more relaxation to contrast requirements while greatly shortening the time-scales over which the system must be stable. This in-turn enables tremendous relief to optical manufacturing, control and stability tolerances bringing them in-line with current technology state of the art. In this paper, we explore a reference design that co-optimizes a large segmented linearized aperture telescope with one-dimensional phase-induced aperture apodization providing high-contrast imaging for spectroscopic analysis. By rotating about a parent star, the chemical signatures of its planets are characterized while affording additional means for background suppression.

Keywords: Exoplanet Spectroscopy, Segmented Space Telescopes, Strip Apertures, PIAA, Mid-Infrared, Coronagraphy

1. INTRODUCTION

There have been many concepts over the years pursuing the objective direct imaging and characterization of exoearths in the visible wavelengths. The Terrestrial Planet Finder Coronagraph (TPFC) mission was an earlier examples that found in the baseline design it must maintain exquisite wavefront error, coating uniformities, contamination control, alignment stability and polarization management [1, 2]. These challenges contrast results drove many advancements in coronagraph designs such as 8th order masks that reduce the sensitivity of dynamic low-order aberrations, the engineering challenges remained daunting and it was not conceivable at that time that TPFC could reasonably consider a segmented primary mirror with the ensuing pico-meter class mechanical alignment stability requirements [3]. The upcoming WFIRST mission seeks to address some aspects of dynamic wavefront control using active sensing approaches their Low-Order Wavefront Sensor (LOWFS), see [4, 5], and future visible concepts such as HabEx and LUVOIR hope to enable segmentation the primary mirror by developing pico-meter class laser metrology trusses to actively stabilize their optical structures [6, 7].

In this paper, we examine an alternative architecture that operates in the mid-infrared showing that it has both substantial engineering and science benefits over visible equivalent concepts. First we revisit and compare the contrast requirements for direct imaging in both visible and Mid-infrared. We then provide the details of our concept that seeks to efficiently achieve the desired observational capabilities while minimizing the hardware required. Finally we show the observational methodology that can be used with concept to fully detect and characterize the exo-planetary system.

2. MINIMIZING CONTRAST REQUIREMENTS

2.1 The Challenges of Direct Imaging

Detecting and characterizing exoearths is challenging. The degree of near-perfection needed in the post-control state of the optical system derives from the contrast required in observing the exoplanet. The stability about these carefully tuned states traces from the faint level of exoplanet light that can be collected. All of this is further worsened by the minute angular separation between exoearths and their parent star. An Earth-Sun analogy at 10-parsec provides only an angular separation of 100 mas.

*Joseph.J.Green@jpl.nasa.gov; www.jpl.nasa.gov

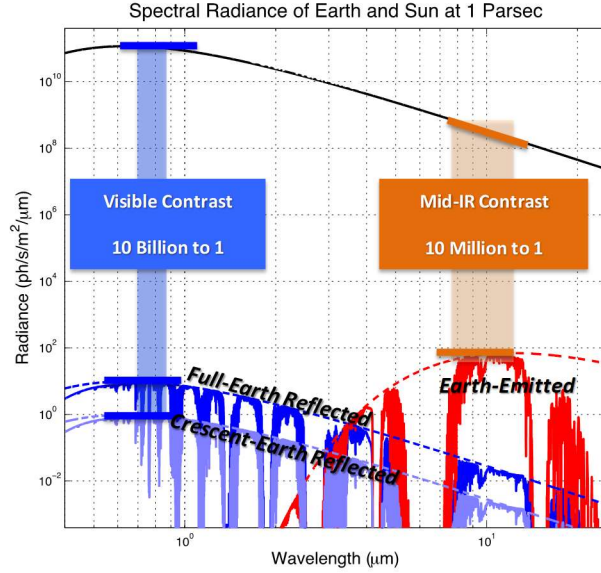


Figure 1: Spectral radiance of an Earth-Sun analog at a range of 1 parsec is shown. At wavelengths around $10\mu\text{m}$ the emitted 300K earthlight is significantly brighter than even a fully illuminated earth-disk in the visible. This combined with the substantially fainter solar radiance, makes the mid-infrared an attractive band to conduct characterization.

Figure 1 explores where there may be better observational opportunities that may provide relief over visible imaging approaches. The black curve in the figure shows the spectral radiance of our Sun from a distance of 1-parsec. At 5800K the Sun has peak radiance at a wavelength around 500nm. The faint blue box represents one the widest bands considered for WFIRST [8]. Covering the oxygen A-band feature, this 700-840nm represents the widest controllable band achievable in their simulations. If other visible bands are desired, the post-coronagraph speckles must be re-controlled to suppress the starlight over the new optical filter

Assuming an average Earth albedo of 0.30, the dark blue curve shows the reflected Earthlight from the full-Earth disk to be 10 billion times fainter that the Sun. In practice, it will be never be possible to observe a full-disk illumination as its Sun would be in the direct line-of-sight between the telescope and the planet. One could imaging that face-on solar systems avoid this and offer season-independent viewing opportunities but their reflected light is further reduced by a factor 2. In general it may be desired to operate down to even crescent-Earth phases where the light is 10x fainter than a fully-illuminated disk (shown by the faint blue curve).

These exoplanet seasonal issues are avoided in the mid-infrared. The red curve shows the thermally emitted planet light dominates the available radiance which is conveniently maximized around planet temperatures of 300K. The faint orange box depicted in Figure 1 shows the 7.5-12.5 μm bandwidth achievable with our mid-infrared concept. In this band, not only is the planet radiance higher but the solar radiance is also diminished. The net contrast is 1000x easier than in the visible. Aside from beneficial contrast requirements, the stronger thermal radiance at $10\mu\text{m}$ greatly shortens timescale over which observations are made. Furthermore, being able to achieve the characterization over the entire band of interest simultaneously is a major time-savings over the band-wise approach necessary in direct visible light characterization.

2.2 Considerations of Temperature and Surface Albedo

Working in the mid-infrared makes the system sensitive to both the star and planet temperature. Table 1 compares the in-band contrast for our Earth-Sun analogy assuming perfectly uniform illumination, surface albedo and temperature. Over the range of conditions explored, the contrast in the mid-infrared remains fairly consistent, ranging from 0.05 to 0.1 million to 1. The contrast in the visible band varies more significantly ranging from 0.05 to 1.5 billion to 1. Only in the case of bright, cold and fully illuminated snow-covered planets did the contrast ratio approach the mid-infrared; still a factor of

36x worse. It is also noteworthy that the apparent brightness of the exoplanet is 15x more sensitive in the visible to surface albedo than in the mid-infrared which may ultimately limit the types of exoearth that are observable.

Figure 2 further explores the impact of the surface temperature of the planet and its parent star. As one may expect, visible coronagraphy is insensitive to these parameters. Mid-infrared contrast, however, improves with increasing planet temperature and decreasing star temperature.

	<i>B1 = 700-840nm</i> <i>B2 = 7.5-12.5um</i>	Planet Temp (K)	Full-Earth Illuminated Contrast		
			B1	B2	Ratio
5750K Star	Average Earth <i>Albedo: B1=30% B2=30%</i>	300	5.2E-10	7.6E-08	146
	Sand Planet <i>Albedo: B1=26% B2=4%</i>	300	4.5E-10	1.0E-07	230
	Water Planet <i>Albedo: B1=3% B2=1%</i>	300	5.2E-11	1.1E-07	2050
	Conifer Planet <i>Albedo: B1=50% B2=1%</i>	300	8.7E-10	1.1E-07	123
	Snow Planet <i>Albedo: B1=90% B2=4%</i>	265	1.6E-09	5.6E-08	36

Table 1: Comparison of Exoearth contrast to its parent star under different surface albedo assumptions shows that even under the most optimistic conditions (full-Earth-disk illumination) there is substantial contrast benefits in the mid-infrared.

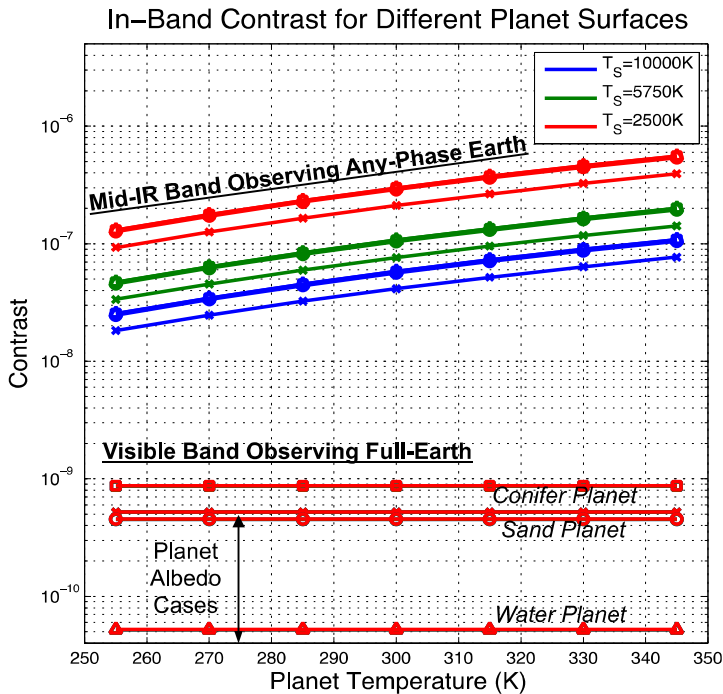


Figure 2: The plot above shows that in the mid-infrared (7.5-12.5μm) the contrast improves with increasing planet temperatures and decreasing star temperatures. While insensitive to planet and star temperatures, at visible wavelengths (0.70-0.84μm) the planet contrast is 100's-1000's times harder depending upon the surface albedo.

3. MID-INFRARED SYSTEM ARCHITECTURE

3.1 Architecture Overview

While we may enjoy relaxed wavefront tolerances with the relaxed contrast, there are two prominent challenges with direct imaging exoearths in the mid-infrared. First, the inner-working angle (IWA) is driven by λ/D and with $\lambda=10\mu\text{m}$, D must grow accordingly. Thus, we are examining approaches that efficiently achieve very large apertures. While we specifically explore 16 and 32 meter sized apertures, the general architectural approach shown is not limited to those specific form factors. The second challenge is thermal. The optics must be in cooled into the 50-60K regime so as not to be inundated with self-emission. While this paper does not address cooling approaches, the compact aperture form factor may lend itself to a conformal layered v-groove radiator sunshade similar to the TPFC concept [3].

As with the earlier TPFC concept, [3], and more recent concepts developed by Rafanelli, [10], and Chakrabari, [11], we are pursuing elongated apertures that provide high-resolution imaging in a principal direction. In our case, we take this to an extreme with a narrow 16x1 and 32x1 meter form factors that along with segmentation to create large neary-one-dimensional telescopes. Figure 3 below shows several views of the optical deign for the 32 meter concept.

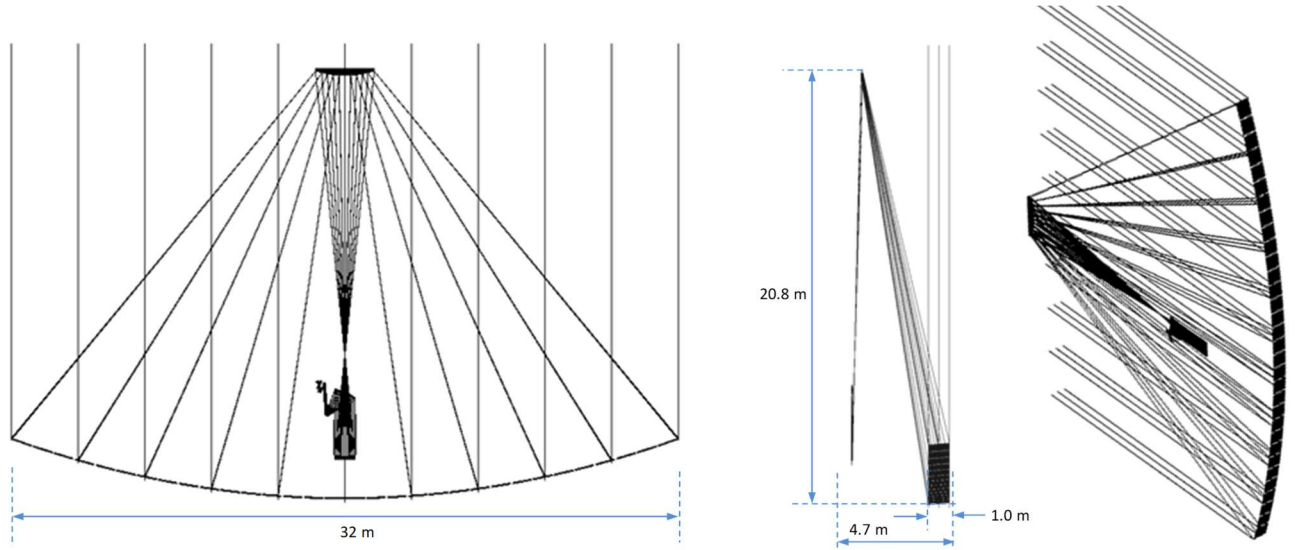


Figure 3: Views of the optical design of the 32m strip-aperture are shown. While very wide in one direction, the 1-meter segments arranged as an off-axis strip-aperture leads to an otherwise compact form factor with an effective F/0.7 primary that has good potential for efficient deployment or on-orbit assemble strategies.

Because we can afford reasonable wavefront and wavefront stability tolerances in the mid-infrared, we can consider segmentation of the primary mirror. As with the James Webb Space Telescope (JWST), segmentation permits to use smaller optics to synthesize the large primary mirror. The effective primary is F/0.7 but the segmentation permits the use of very slow F/22.4 1x1 meter segments. The telescope is slightly off-axis and has all subsequent optics arrange to fit neatly into a tower next to the primary array. Although not shown here, we plan to employ laser-trusses around the segments to stabilize to architecture. As we will show later, the requirements on the laser-metrology will likely be in 1-5nm rms regime, akin to current state of the art [12].

Figure 4 shows the overall system block diagram. The optical telescope assembly is followed by a 4-mirror 1/32x anamorphic afocal group that produces a 31x31 mm emerging beam, i.e. it converts the 1000 mm beam to 31 mm in one direction, and retains the 31 mm size in the other direction. This group also maintains a common exit pupil location in the two orthogonal directions. This exit pupil is virtual however, so to create an accessible pupil at a deformable mirror, an

additional 3-mirror afocal pupil relay follows the anamorphic group. Following the deformable mirror is an beam-reformatting afocal group in the system. The optics that follows are for starlight suppression.

One of the most challenging aspects of direct exoplanet characterization is suppression of the starlight so that high quality measurements of the planet light can be conducted. Here we follow similar principals to the Phase Induced Aperture Apodization (PIAA) approach that was introduced to the exoplanet community by Guyon [13]. We will describe this in more detail in the next section. After the starlight is eliminated, the residual planet light is passed on to either an imaging camera or spectrometer via a selection mirror.

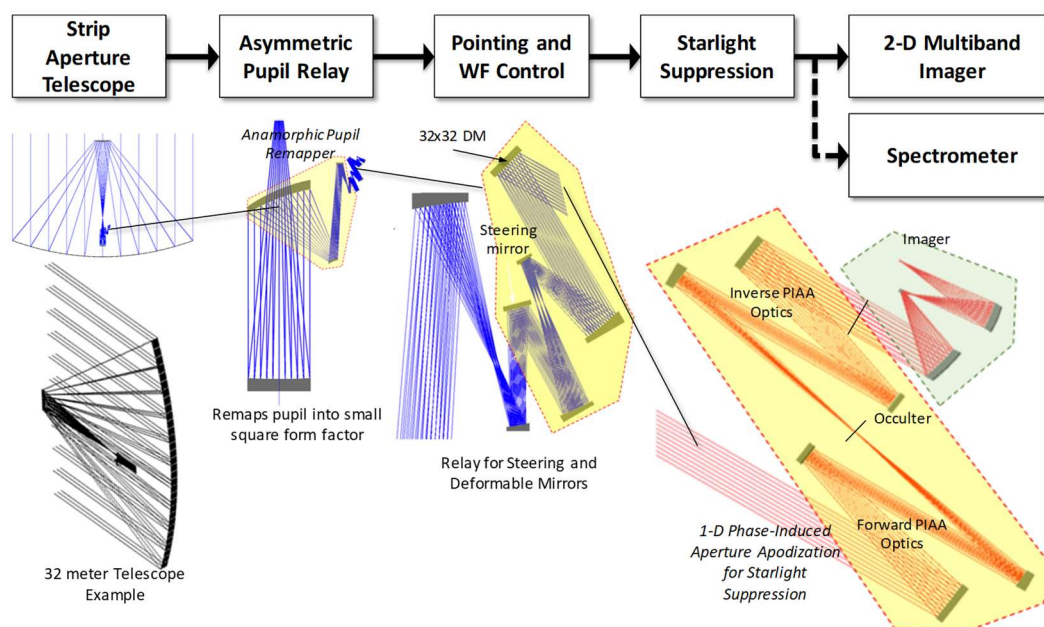


Figure 4: Block diagram depicting the general architecture of the mid-infrared 32 meter concept is shown. Below the diagram are the optical ray traces of the key subsystems ending in the imager. The spectrometer ray trace is not shown.

3.2 Starlight Suppression

In Figure 5, we shown a more detailed view of our preferred starlight suppression approach. We chose the PIAA method to enable tight IWA performance while maximally preserving the incoming planet light. Unlike the recently high-performance demonstration of PIAA optics [14], we use a cylindrical optics to conduct a strictly 1-dimensional remapping of the incoming collimated light into a Gaussian intensity profile. This produces a star point-spread-function (PSF) with greatly suppressed side-lobes in the high-resolution direction of the aperture. The star PSF is largely eliminated by the subsequent $1.4 \lambda/D$ linear-bar occulting spot placed at focus.

A well know issue with PIAA is that the highly non-uniform remapping induces significant off-axis aberrations. Even an ideally tilted wavefront from an off-axis source is warped by the remapping creating significant wavefront that grows with the tilt. Oddly, this actually acts as a benefit to PIAA as some additional light from the planet PSF gets scattered outside the occulter support. After re-collimation, the residual star and planet light are remapped though an inverse PIAA pair to reduce the tilt-induced aberrations and recover the Strehl of the planet PSF.

In Figure 6, we show the fraction of the planet PSF core that is preserved by the end-to-end starlight suppression system as a function of field angle for both the 16 and 32 meter concepts. Even though the occulter is sized to be $1.4 \lambda/D$, we are able to maintain at least half the maximum planet full-width-half-max (FWHM) down to even $1.0 \lambda/D$ permitting the 32 meter concept to work at close as 65mas to the parent star.

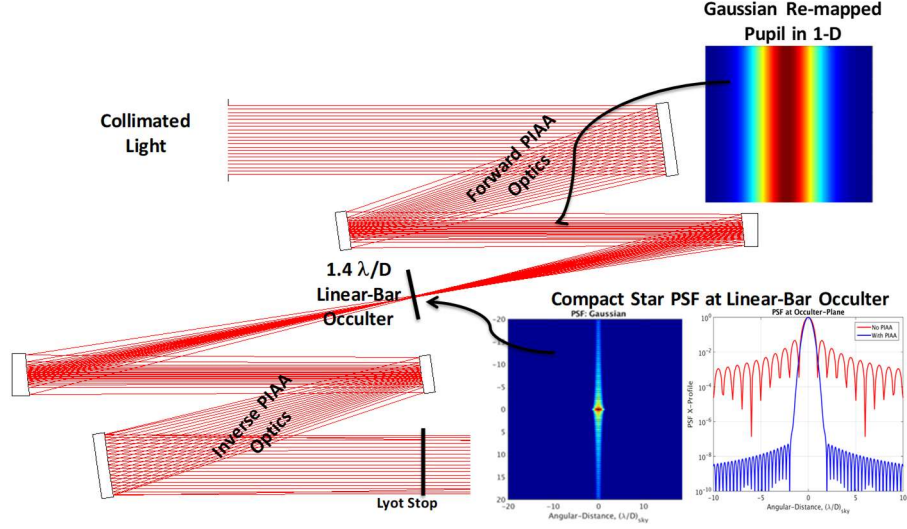


Figure 5: Detail of the starlight suppression system ray-trace is shown. The forward PIAA optics re-map the high-resolution direction of the incoming collimated light into a 1-D Gaussian profile. The resulting stellar diffraction pattern is largely eliminated by the subsequent linear-bar occulting spot. After re-collimation, the residual star and planet light are remapped again to preserve the Strehl of the planet PSF.

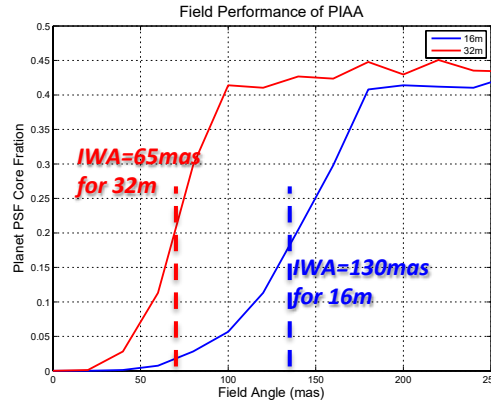


Figure 6: The inner working angle performance is shown for both a 16 and 32 meter versions of the architecture concept. The Planet PSF Core Fraction is measured as the fraction of the integrated energy within the full-width-half-max compared to the total. At a 50% drop in this metric, the 16m and 32m systems can achieve an IWA of 130mas and 65mas respectively.

3.3 Achieving and Maintaining Contrast Performance

With the single deformable mirror (DM) we control the residual starlight over half of the telescope field using the electric-field-conjugation (EFC) approach [15, 16] to minimize the residual static speckles. Rather than use the entire half-field, however, we further restrict EFC control objective to a slim $1\text{-}\lambda/D$ wide strip along the length of the high resolution direction on one side of the field. This is shown in Figure 7 as the ‘Controlled Dark Hole’. We find that by limiting the control objective this aggressively, we are able to exploit all the control degrees of freedom of a 32×32 actuator DM to suppress the residual starlight over a full $7.5\text{-}12.5\text{ }\mu\text{m}$ band to enable fully wideband spectroscopy.

Figure 7 also shows the impact of uncontrolled segment aberration evolving during the observations. Here we placed random realizations of low-order surface deformations onto each segment to represent a highly stressing condition for dynamic wavefront error. In visible coronagraphy, such error terms would have to be held at pico-meter levels to avoid overwhelming the planet light with newly leaked starlight. In our mid-infrared concept, however, we can tolerate $5\text{-}10\text{nm}$

rms changes in the wavefront after the dark-hole has been controlled. This is a major benefit to mid-infrared concepts as it permits the use conventional mirror fabrication technologies and laser-metrology trusses that are within our current state of the art.

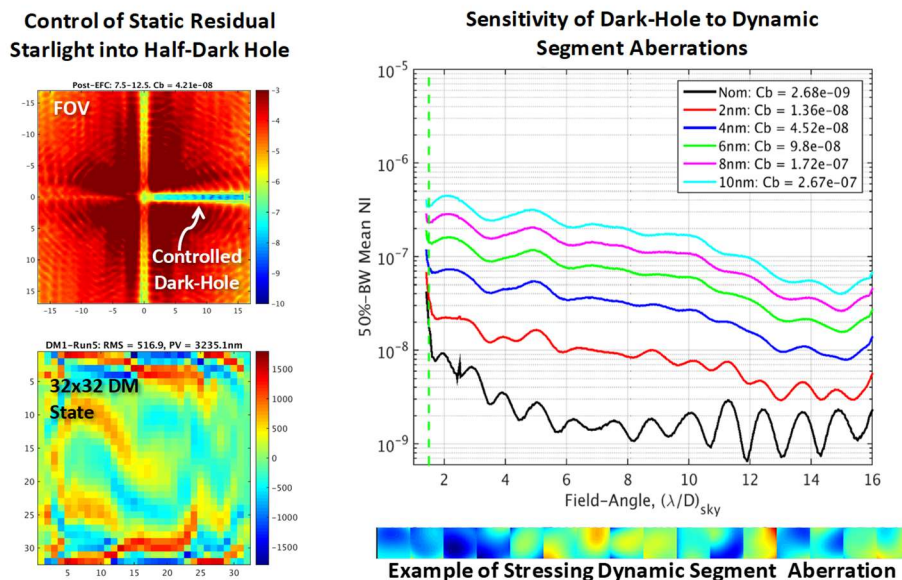


Figure 7: The controlled half-dark hole over full 7.5-12.5μm band is shown (upper-left) using a 32x32 actuator deformable mirror whose control state is also illustrated (lower-left). If the aberration content of the wavefront is permitted to evolve during the observation, the contrast floor grows (upper-right). Depending upon budgeted contrast, the system can tolerate 5-10nm of segment shape deformation while maintaining leaked starlight at similar levels to the zodi+exo-zodi backgrounds.

4. OBSERVATION CONCEPT

4.1 Scanning Approach

To make best use of the strip of controlled speckles, we choose to observe continuously as the system slowly rotates while pointing to the parent star. We assume the instruments, telescope and bus rotate rigidly together as the scan is conducted. Figure 8 illustrates that as the system rotates, the controlled FOV about the parent star as rotates permitting a full-field scan. Placing a slit-spectrometer, similar to JPL's HyTES instrument [17], in alignment to the dark-hole, the entire FOV containing planetary system may be characterized.

Figure 9 depicts this spectroscopic scanning concept. As the rotation is completed, the resulting data forms a 'hyper-cylinder' with its disk covering the field of view and the length containing the spectral sampling of every field-point measured about the parent star. Planets near the center of rotation will get oversampled compared to those as the edge of the FOV. The highly asymmetric aspect ratio of the aperture yields a planet PSF with large side-lobes in the low-resolution direction of the telescope. The elongated planet PSF core and its side-lobes, leak into the instrument over a significant range of telescope orientations. This is also illustrated in right side of Figure 9. The presence of the planet spectrum will thus appear at strengths and locations that will depend on its separation for the parent star and the relative orientation of the aperture. This may all be accounted for in the post-processing of the hyper-cylinder data to produce the optimal estimate of the planetary spectrum. One approach we are considering is an extension to the Poisson Maximum a-Posteriori algorithm with which we had earlier explored aperture synthesis or rotating strip apertures [18].

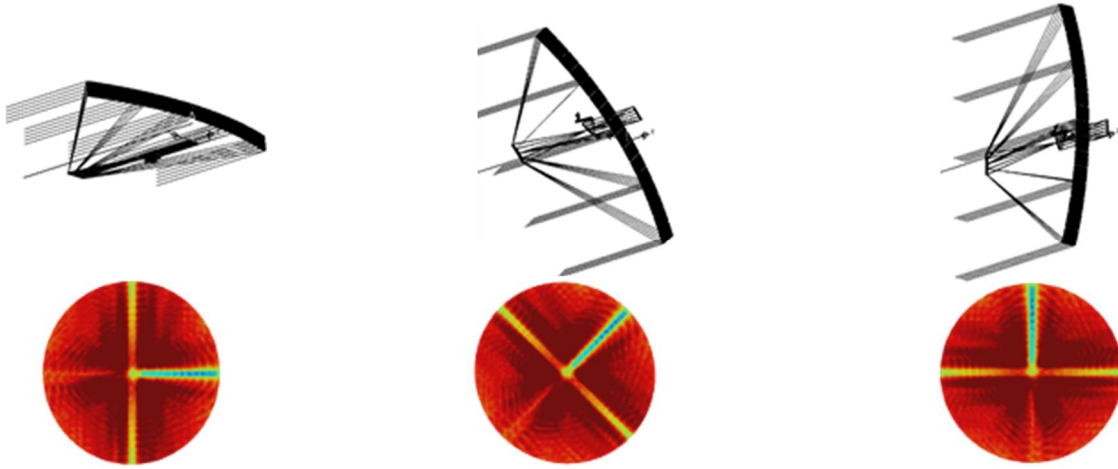


Figure 8: As the system slowly rotates while staring at the parent star, the half-dark-hole sweeps out the field of view that extends well-beyond the habitable zone. Over the course of a full-rotation, the planetary system under study is fully and efficiently characterized.

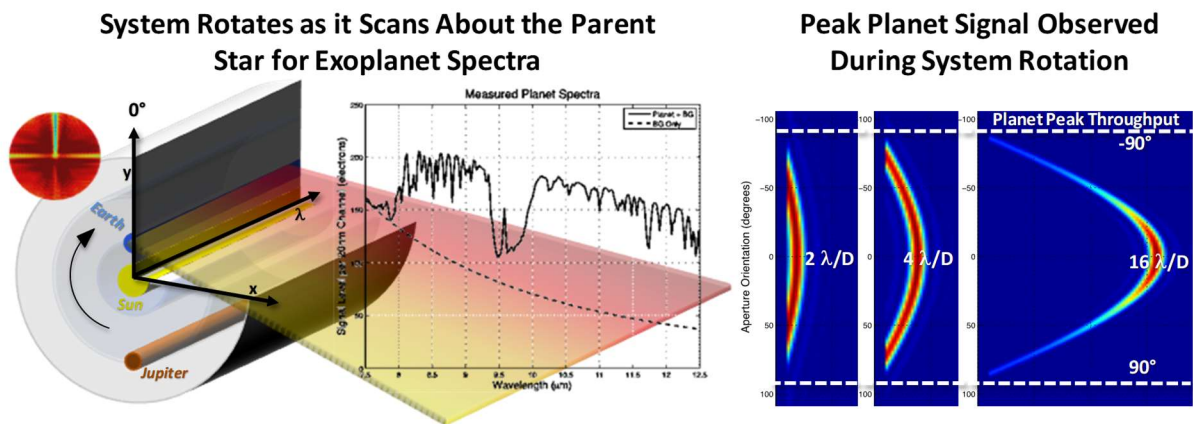


Figure 9: Placing a slit spectrometer behind the dark-hole is one approach to enable spectroscopic analysis of the entire planetary system. The left diagram is an illustration of the hyper-cylinder of data collected as the telescope rotation sweeps out the field of view. As shown on the right, the highly asymmetric PSF from the aperture aspect ratio causes off-axis planet light to leak into the instrument field proving for a significant oversampling of the planet signal particularly for planets at small working angles.

4.2 Characterization Opportunities

A spectroscopic benefit of working in the mid-infrared comes in the form of the separability of the planet spectrum from the zodiacal, exo-zodiacal and residual starlight. All of these non-planetary terms are anticipated to be very smooth functions in the 7.5-12.5 μ m band enabling robust detection filters and spectral retrieval method. Figure 10, shows an example of a measured spectrum assuming a mid-infrared instrument with 20nm per channel of an Earth-Sun analogy at 1 parsec.

The spectrum shown is the result taking the top-of-atmosphere transmission from a nadir view geometry in MODTRAN that is configured for standard Rural Mid-Latitude Summer Earth atmospheric model. The resulting radiance is mainly from the upwelling self-emission of the Earth surface being filtered by these atmospheric model. For the 1-parsec simulation we assume the entire Earth disk integrates uniformly into the radiance driving the planet PSF. In future

simulations, we plan to account for the additional modulation depth of the atmosphere resulting from the integral over all of viewing geometries to account for the additional air-mass dependencies.

On top of the simulated spectrum shown in Figure 10, we placed lines to represent regions where modulation occurs for many of the key atmospheric chemicals of interest to exoplanetary science. As with the airborne spectroscopy conducted with HyTES, we envision a similar chain of analysis where the atmosphere constituents are retrieved and residual be further decomposed into surface emissivity and temperature products. The emissivity product itself, of course, can be further decomposed into solids such as silicates and oxides. Because the system is very efficient at fully scanning the exoplanetary system of interest, these scans can be repeated many times over the seasons, observing varying exoplanet climates and surface properties.

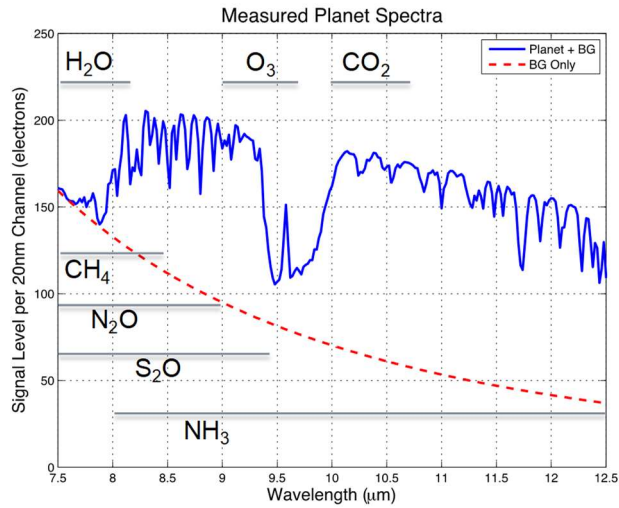


Figure 10: Simulation of a measured spectrum for an Earth at 1 parsec is shown assuming a 16x1 meter aperture and a spectrometer with 20nm per channel. The observation also assumes 36 seconds per frame and a 60 minute total scan for the 360 degree field about the parent star. As shown by the linear bars, many important atmospheric chemicals are detectable within this band.

To explore the sizing of the aperture, we looked at a list of our neighboring stars. Table 2, shows how potential exoearths at 1 AU from their parent star map into both the 16 and 32 meter versions of our concept. Using the Planet PSF Core throughput as a guide, we color coded the lists accordingly to help highlight the systems characterization potential. The 16 meter concept offers good access out to 9.2 parsecs (30 light years) and covers our nearest 45 stars. The 32 meter concept can characterize exoearths out to 60 light years which covers more than 600 neighboring stars. Even beyond that, the large system can characterize exo-Jupiters out to 300 light years providing access to more than 250,000 star systems.

Relative Planet Core Throughput				Relative Planet Core Throughput				Relative Planet Core Throughput			
Star	Parsecs	16m	32m	Star	Parsecs	16m	32m	Star	Parsecs	16m	32m
1 Alpha Centauri	1.35	1.00	1.00	41 Gamma Leporis	8.97	0.60	1.00	81 85 Pegasi	12.40	0.03	1.00
2 Alpha Canis Majoris	2.64	1.00	1.00	42 Delta Eridani	9.04	0.56	1.00	82 Rho- π Cancri	12.53	0.03	1.00
3 Epsilon Eridani	3.22	1.00	1.00	43 Beta Comae Berenices	9.16	0.52	1.00	83 HR3259	12.58	0.03	1.00
4 Alpha Canis Minoris	3.50	1.00	1.00	44 HR4550	9.16	0.52	1.00	84 HR483	12.64	0.02	1.00
5 61 Cygni	3.50	1.00	1.00	45 Kappa- π Ceti	9.16	0.52	1.00	85 Lambda Aurigae	12.64	0.02	1.00
6 Epsilon Indi	3.63	1.00	1.00	46 Gamma Pavonis	9.22	0.49	1.00	86 HR683	12.68	0.02	1.00
7 Tau Ceti	3.65	1.00	1.00	47 HR4523	9.24	0.48	1.00	87 44 Bov δ tis	12.76	0.02	1.00
8 Omicron- ς Eridani	5.04	1.00	1.00	48 HR4458	9.54	0.37	1.00	88 HR6518	12.80	0.02	1.00
9 70 Ophiuchi	5.09	1.00	1.00	49 61 Ursae Majoris	9.54	0.37	1.00	89 36 Ursae Majoris	12.85	0.02	1.00
10 Alpha Aquilae	5.14	1.00	1.00	50 12 Ophiuchi	9.78	0.30	1.00	90 HR6094	12.87	0.02	1.00
11 Sigma Draconis	5.77	1.00	1.00	51 HR511	9.98	0.25	1.00	91 HR4587	12.91	0.02	1.00
12 HR5568	5.91	1.00	1.00	52 HR5256	10.11	0.22	1.00	92 Alpha Aurigae	12.94	0.02	1.00
13 Eta Cassiopeiae	5.95	1.00	1.00	53 Alpha Mensae	10.15	0.21	1.00	93 HR6998	12.98	0.02	1.00
14 36 Ophiuchi	5.98	1.00	1.00	54 Beta Geminorum	10.34	0.18	1.00	94 58 Eridani	13.32	0.01	1.00
15 HR7703	6.05	1.00	1.00	55 HR857	10.38	0.17	1.00	95 Upsilon Andromedae	13.47	0.01	1.00
16 82 Eridani	6.06	1.00	1.00	56 Iota Persei	10.53	0.15	1.00	96 Theta Ursae Majoris	13.49	0.01	1.00
17 Delta Pavonis	6.11	1.00	1.00	57 HR9038	10.79	0.12	1.00	97 HR8501	13.61	0.01	1.00
18 HR8832	6.52	1.00	1.00	58 Zeta Herculis	10.80	0.12	1.00	98 HR8	13.70	0.01	1.00
19 Xi Bov δ tis	6.70	1.00	1.00	59 Delta Trianguli	10.85	0.11	1.00	99 Beta Aquilae	13.71	0.01	1.00
20 HR753	7.21	0.99	1.00	60 Beta Virginis	10.90	0.11	1.00	100 10 Tauri	13.72	0.01	1.00
21 HR6426	7.24	0.99	1.00	61 HR637	10.91	0.10	1.00	101 Iota Piscium	13.79	0.01	1.00
22 HR222	7.46	0.98	1.00	62 Beta Leonis	11.09	0.09	1.00	102 Gamma Cephei	13.79	0.01	1.00
23 107 Piscium	7.47	0.98	1.00	63 HR6806	11.10	0.09	1.00	103 Tau- π Eridani	13.97	0.01	0.99
24 Beta Hydri	7.47	0.98	1.00	64 54 Piscium	11.11	0.09	1.00	104 18 Scorpii	14.02	0.01	0.99
25 Mu Cassiopeiae	7.55	0.97	1.00	65 Gamma Serpentis	11.12	0.09	1.00	105 47 Ursae Majoris	14.08	0.01	0.99
26 HR8721	7.64	0.97	1.00	66 11 Leonis Minoris	11.18	0.08	1.00	106 26 Draconis	14.09	0.01	0.99
27 Alpha Piscis Austrini	7.69	0.96	1.00	67 Gamma Leporis	11.53	0.06	1.00	107 Alpha Formacis	14.11	0.01	0.99
28 Alpha Lyrae	7.76	0.95	1.00	68 Delta Eridani	11.63	0.06	1.00	108 HR7578	14.22	0.01	0.99
29 Pi- ζ Orionis	8.03	0.91	1.00	69 Beta Comae Berenices	11.73	0.05	1.00	109 Pi- π Ursae Majoris	14.27	0.01	0.99
30 Chi Draconis	8.06	0.91	1.00	70 HR4551	11.84	0.05	1.00	110 Alpha Ophiuchi	14.32	0.01	0.99
31 ρ Eridani	8.15	0.89	1.00	71 Kappa- π Ceti	11.94	0.04	1.00	111 Eta Cephei	14.34	0.01	0.99
32 Xi Ursae Majoris	8.34	0.84	1.00	72 Gamma Pavonis	12.04	0.04	1.00	112 72 Herculis	14.39	0.01	0.99
33 Beta Canum Venaticorum	8.37	0.83	1.00	73 HR4393	12.14	0.04	1.00	113 Nu- ς Lupi	14.56	0.01	0.99
34 Mu Herculis	8.40	0.82	1.00	74 HR4328	12.24	0.03	1.00	114 Theta Bov δ tis	14.57	0.01	0.99
35 61 Virginis	8.53	0.78	1.00	75 62 Ursae Majoris	12.34	0.03	1.00	115 Iota Ursae Majoris	14.64	0.01	0.98
36 Zeta Tucanae	8.59	0.75	1.00	76 13 Ophiuchi	12.45	0.03	1.00	116 HR7898	14.65	0.01	0.98
37 Chi- π Orionis	8.66	0.72	1.00	77 HR10001	12.55	0.03	1.00	117 111 Tauri	14.66	0.01	0.98
38 HR6416	8.79	0.67	1.00	78 HR14746	12.65	0.02	1.00	118 Psi Serpentis	14.67	0.01	0.98
39 HR1614	8.81	0.66	1.00	79 Alpha Mensae	12.75	0.02	1.00	119 Psi Capricorni	14.67	0.01	0.98
40 HR7722	8.82	0.66	1.00	80 Beta Geminorum	12.85	0.02	1.00	120 Alpha Corvi	14.77	0.01	0.98

Table 2: Sample performance of the 16 and 32 meter concepts against our nearest neighbors is shown above. The colorization reflects the planet throughput with field-angle. The 16meter concept can characterize systems with planets a 1 AU or more out to 30 light years. The 32 meter concept can characterize out to 60 light years.

5. CONCLUSION

In this paper, we introduced a new architecture for exoearth characterization in the mid-infrared. By linearizing and segmenting the primary mirror we hope to enable affordable large scale systems that can offer excellent science potential while maintaining their engineering requirements to within the current state-of-the art. The contrast and shear brightness of exoearths in the mid-infrared are clear drivers for relaxing requirements on both the achieved wavefront quality of the system as well as its stability magnitudes and timescales. Mid-infrared also has the distinct advantages of enabling direct measurements independent of exoplanet season while enabling wideband access to many key spectral signatures. These measurements can be done rapidly and repeated over the exoplanet year. As the planets present new-faces to be analyzed, the surface and atmospheric decompositions may reveal the presence of clouds, oceans and land-masses. The surface temperatures retrieved may also help estimate planet core temperatures from the passive heating from due to its star. The mid-infrared concepts shown provide the best opportunities for exoearth characterization.

6. ACKNOWLEDGMENTS

The research was carried out at the Jet Propulsion Laboratory, California Institute of Technology, under a contract with the National Aeronautics and Space Administration.

REFERENCES

- [1] Mary L. White, Stuart B. Shaklan, P. Douglas Lisman, Timothy Ho, Pantazis Mouroulis, Scott A. Basinger, William Ledebor, Eug-Yun Kwack, Andrew Kissil, Gary E. Mosier, Alice Liu, Chuck Bowers, Carl Blaurock, Terry Cafferty, "Design and performance of the Terrestrial Planet Finder coronagraph", Proc. SPIE 5487, Optical, Infrared, and Millimeter Space Telescopes, (12 October 2004);
- [2] Stuart B. Shaklan and Joseph J. Green, "Reflectivity and optical surface height requirements in a broadband coronagraph. 1. Contrast floor due to controllable spatial frequencies," Appl. Opt. 45, 5143-5153 (2006)
- [3] V. G. Ford, A. B. Hull, S. B. Shaklan, M. B. Levine, M. L. White, A. E. Lowman, and E. J. Cohen, "Terrestrial Planet Finder Coronagraph," in Techniques and Instrumentation for Detection of Exoplanets, D. R. Coulter, ed., Proc. SPIE 5170, 1–12 (2003).
- [4] Fang Shi, *et al*, "Low order wavefront sensing and control for WFIRST Coronagraph," Proc. SPIE, vol. 9904, pp. 990418, August 2016.
- [5] Fang Shi, *et al*, "Dynamic testbed demonstration of WFIRST coronagraph low order wavefront sensing and control (LOWFS/C)," Proc SPIE (Austin, TX), in preparation (2018).
- [6] Stuart B. Shaklan, Luis F. Marchen, Feng Zhao, Robert D. Peters, Timothy Ho, Buck Holmes, "Metrology system for the Terrestrial Planet Finder Coronagraph", Proc. SPIE 5528, Space Systems Engineering and Optical Alignment Mechanisms, (30 September 2004).
- [7] Joel A. Nissen, Alireza Azizi, Feng Zhao, Shannon Kian G. Zareh, Shanti R. Rao, Jeffrey B. Jewell, Dustin Moore, "Laser metrology for ultra-stable space-based coronagraphs", Proc. SPIE 10398, UV/Optical/IR Space Telescopes and Instruments: Innovative Technologies and Concepts VIII, 103980I (5 September 2017);
- [8] K. Balasubramanian, *et al*, "WFIRST-AFTA coronagraph shaped pupil masks: design, fabrication, and characterization," J. Astron. Telesc. Instrum. Syst. 2(1) 011005 (7 December 2015)
- [9] Erkin Sidick, Byoung-Joon Seo, Brian Kern, David Marx, Ilya Poberezhskiy, and Bijan Nemati, "Optimizing the Regularization in Broadband Wavefront Control Algorithm for WFIRST Coronagraph," Proc. SPIE, vol. 10400, vol. pp.1040022-1, August 2017.
- [10] Gerard L. Rafanelli, Christopher M Cosner, Susan B. Spencer, Douglas Wolfe, Arthur Newman, Ronald Polidan, Supriya Chakrabarti, "Revolutionary astrophysics using an incoherent synthetic optical aperture", Proc. SPIE 10398, UV/Optical/IR Space Telescopes and Instruments: Innovative Technologies and Concepts VIII, 103980P (5 September 2017).
- [11] S. Chakrabarti, *et al*, Rotatable Aperture Coronagraph for Exoplanetary Studies (RACES), AAS 231, Washington DC (2018).
- [12] R. Goullioud, C. A. Lindensmith, I. Hahn, "Results from SIM's thermo-opto-mechanical (TOM3) testbed", Proc. SPIE 6268, Advances in Stellar Interferometry, 626824 (28 June 2006).
- [13] Olivier Guyon, "Phase-induced amplitude apodization of telescope pupils for extrasolar terrestrial planet imaging," A&A 404, 379–387 (2003).
- [14] Olivier Guyon, Brian Kern, Ruslan Belikov, Stuart Shaklan, Andreas Kuhnert, Amir Give'on, "Phase-Induced Amplitude Apodization (PIAA) coronagraphy: recent results and future prospects," Proc. SPIE 8151, Techniques and Instrumentation for Detection of Exoplanets V, 81510H (15 September 2011).
- [15] Amir Give'on, Brian Kern, Stuart Shaklan, Dwight C. Moody, Laurent Pueyo, "Broadband wavefront correction algorithm for high-contrast imaging systems", Proc. SPIE 6691, Astronomical Adaptive Optics Systems and Applications III, 66910A (18 September 2007).
- [16] Amir Give'on, "A unified formalism for high contrast imaging correction algorithms," Proc. SPIE 7440, Techniques and Instrumentation for Detection of Exoplanets IV, 74400D (19 August 2009).
- [17] William R. Johnson, Glynn Hulley, Simon J. Hook, "Remote gas plume sensing and imaging with NASA's Hyperspectral Thermal Emission Spectrometer (HyTES).", Proc. SPIE 9101, Next-Generation Spectroscopic Technologies VII, 91010V (28 May 2014).
- [18] J. J. Green and B. R. Hunt, "Super-resolution in a synthetic aperture imaging system," Proceedings of International Conference on Image Processing, Santa Barbara, CA, 1997, pp. 865-868 vol.1.